PERGAMON

International Journal of Solids and Structures 40 (2003) 6267–6284

INTERNATIONAL JOURNAL OF SOLIDS and STRUCTURES

www.elsevier.com/locate/ijsolstr

Effect of specimen size and crack depth on 3D crack-front constraint for SENB specimens

Y. Kim, Y.J. Chao *, X.K. Zhu

Department of Mechanical Engineering, University of South Carolina, 300 S. Main, Columbia, SC 29208, USA

Received 16 June 2003; received in revised form 16 June 2003

Abstract

Three-dimensional (3D) elastic–plastic finite element analyses (FEA) are performed to study constraint effect on the crack-front stress fields for single-edge notched bend (SENB) specimens. Both rectangular and square cross-section of the specimens with a deep crack of $a/W = 0.5$ are considered to investigate the effect of specimen size. A square-cross-section specimen with a shallow crack of $a/W = 0.15$ is also considered to examine the effect of crack depth. Stresses from FEA at the crack front on different planes of the specimen are compared with those determined by the J–A_2 three-term solution. Results show that in-plane stress fields can be characterized by the three-term solution throughout the thickness even in the region near the free surface. Cleavage fracture toughness data is compared to predict the effects of specimen size and crack depth on fracture behavior. It is found that the distributions of crack opening stress are nearly the same for the SENB specimens at the critical J which is consistent with the RKR model. Furthermore our results indicate that there is a distinct relationship between the crack-front constraint and the cleavage fracture toughness. By introducing the failure curves, the minimum fracture toughness and scatter band can be well captured using the J–A_2 approach.

Keywords: Constraint effect; SENB; FEA; Three dimension; Crack-front field; Cleavage fracture toughness

1. Introduction

Fracture toughness has been considered as a *material property*, which means it should be independent of size and geometry. Most of the current integrity analyses are based on this property. However, it has been found that fracture toughness depends on the specimen size, crack depth, geometry, and loading condition. These effects have been attributed to different crack-front constraint. As a result, it is questionable to apply the fracture toughness value determined from small laboratory specimens to the integrity assessment of large defected structures.

* Corresponding author. Tel.: +1-803-777-5869; fax: +1-803-777-0106.
E-mail address: chao@sc.edu (Y.J. Chao).

0020-7683/$ - see front matter © 2003 Elsevier Ltd. All rights reserved.
doi:10.1016/S0020-7683(03)00392-5

Several theories and approaches have been proposed to predict the specimen size and crack depth dependence on fracture toughness and to quantify the crack-front constraint against the plastic flow. Among them, three representatives are the J–T theory proposed by Betegon and Hancock (1991), the J–Q theory developed by O'Dowd and Shih (1991, 1992), and the J–A_2 three-term solution developed by Yang et al. (1993a,b) and Chao et al. (1994).

The present work is concerned with the application of the J–A_2 three-term solution (hereinafter called the J–A_2 solution) to 3D crack-front stress field and the interpretation of cleavage fracture for single-edge notched bend (SENB) specimens. Yang et al. (1993a,b) and Chao et al. (1994) have carried out a complete analysis of higher-order crack-front fields in power-law hardening materials. A three-term expansion they developed is controlled only by two parameters, namely J and A_2. The three-term asymptotic stress field can be written as

$$\frac{\sigma_{ij}}{\sigma_0} = A_1\left[\left(\frac{r}{L}\right)^{s_1}\tilde{\sigma}_{ij}^{(1)}(\theta) + A_2\left(\frac{r}{L}\right)^{s_2}\tilde{\sigma}_{ij}^{(2)}(\theta) + A_2^2\left(\frac{r}{L}\right)^{s_3}\tilde{\sigma}_{ij}^{(3)}(\theta)\right] \tag{1}$$

where σ_0 is a reference stress that is generally equal to the yield stress, the angular functions $\tilde{\sigma}_{ij}^{(k)}$ $(k = 1,2,3)$ and the stress power exponents s_k $(s_1 < s_2 < s_3)$ are only dependent of the hardening exponent n and independent of the other material constants and the applied loads. L is a characteristic length parameter which can be chosen as the crack length a, the specimen width W, or the thickness B. The parameters A_1 and s_1 from the HRR fields (Hutchinson, 1968; Rice and Rosengren, 1968) are given by

$$A_1 = \left(\frac{J}{\alpha\varepsilon_0\sigma_0 I_n L}\right)^{-s_1}, \quad s_1 = -\frac{1}{n+1} \tag{2}$$

and $s_3 = 2s_2 - s_1$ for $n \geqslant 3$. In Eq. (2), J is the J-integral by Rice (1968), α is a material hardening constant, ε_0 is the yield strain, n is the strain hardening exponent, I_n is an integration constant that depends on n. A_2 is an undetermined parameter and may be related to the loading and geometry of the specimen. The non-dimensional functions and s_2 in Eq. (1) are given in a report written by Chao and Zhang (1997). Zhu and Chao (1999) have extended the three-term solution to non-hardening materials. How the mathematical solution of Eq. (1) can be used for a two parameter fracture testing is presented in Chao and Zhu (1998). The J–A_2 concept has also been extended to quantify the constraint effect on J-resistance curves (Chao and Zhu, 2000).

Most studies on constraint effects have been carried out for two-dimensional (2D) crack problems; but not for 3D. One difficulty on the 3D crack analysis lies in the enormous computational expenses besides the complex character of the stress and strain fields at a 3D crack front. Recently, the authors showed that 3D crack-front fields in a thin plate are well represented by the J–A_2 three-term solution under SSY and LSY conditions (Kim et al., 2001; Zhu et al., 2001).

As an extension of our previous studies on the 3D crack-front field of thin plate, current work is aimed to quantify the level of 3D crack-front constraint in thick SENB specimens. The J–A_2 solution is applied to characterize the crack-front constraint effect on cleavage fracture toughness. To study the effect of specimen size, two SENB specimens, one with square and the other with rectangular cross-section, having $a/W = 0.5$ (simply referred to as deep square specimen and rectangular specimen) are considered. In order to examine the effect of crack depth, another square-cross-section SENB specimen having a shallow crack of $a/W = 0.15$ (hereinafter called shallow square specimen) is also considered. All the specimens have the same thickness, B. The rectangular specimen has the width, W, equal to twice the thickness, $W = 2B$, while both the deep square and shallow square specimens have $W = B$. The span of each specimen is four times of the specimen width. Consequently, the volume of the rectangular specimen is four times as large as that of the square specimen.

2. Computational procedures

3D elastic–plastic FEA are conducted using the commercial FEA code, ABAQUS (1998). All the SENB specimens use the similar FEA mesh as shown in Fig. 1. The size of the square specimens is $31.8\times31.8\times127$ mm (thickness × width × span, $B \times W \times S$), and the rectangular specimen is $31.8\times63.6\times254$ mm. A deep crack with $a/W = 0.5$ is considered for both the square and rectangular specimens. Shallow crack ($a/W = 0.15$) is considered only for the square specimen. The square specimens have the same size as those used by Sorem et al. (1989) and the rectangular specimen used by Wellman et al. (1988).

The FEA calculations in this work are based on the J_2 incremental theory of plasticity. A similar coordinate system is employed for all the specimens such that the x-axis lies in the crack plane and is normal to the straight crack front; y-axis is orthogonal to the crack plane and the z-axis lies on the thickness direction. The origin of the coordinate system is located at the crack tip on the center plane. Only a quarter of the specimen (region $0 \leqslant \theta \leqslant \pi$, $0 \leqslant z \leqslant 1/2t$) is modeled due to the symmetry with respect to the mid-plane ($z = 0$) and the crack surface plane ($y = 0$). Along the thickness direction (z-axis), the identical planar mesh is repeated from the symmetry plane (i.e. mid-plane, $z = 0$) to the free surface ($z/t = 0.5$). In order to catch the drastic change of the stress field near the free surface, thickness of successive element layer is exponentially reduced from the mid-plane toward the free surface. 20-node quadratic brick elements with reduced integration and seven element layers throughout the half thickness are used. Within each layer, 30 focused rings of elements encompass the crack front for the deep square and the rectangular specimens and 20 elements for shallow square specimen. The size of each ring increases gradually with the radial distance from the crack tip. The size of the smallest element for the deep square, rectangular, and shallow square specimens are 1.08×10^{-4}, 2.16×10^{-4}, and 3.06×10^{-4} of the thickness respectively. In the circumferential direction, 24 equally sized elements are defined in the angular region from 0 to π.

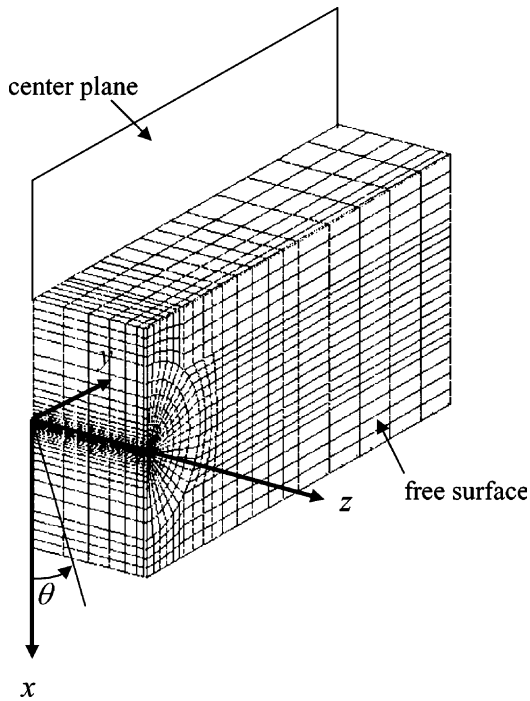

Fig. 1. Finite element mesh for the SENB specimens.

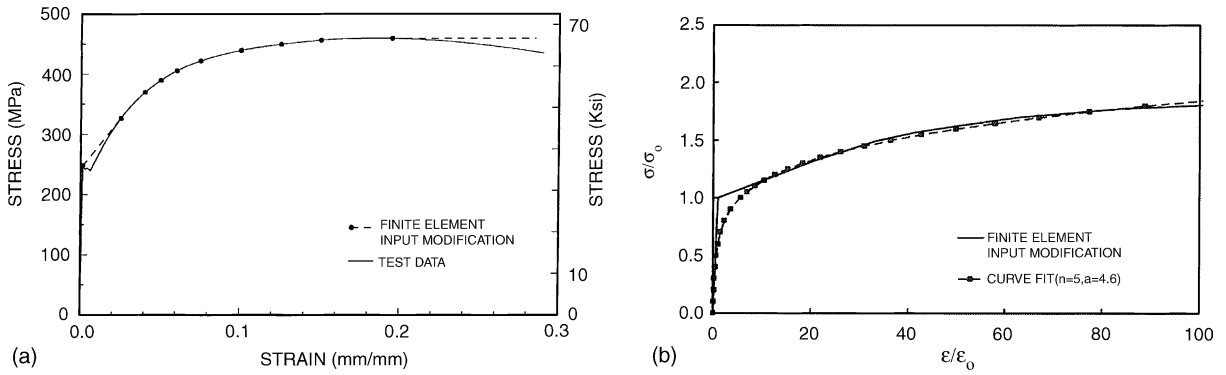

Fig. 2. Tensile test data for A36 steel: (a) modified test data for FEA, (b) curve fit to the Ramberg–Osgood constitutive equation.

The material considered here is the low-strength structural steel A36. The tensile test result and the input data used for FEA is reproduced in Fig. 2(a) (Sorem, 1989). For the application of the J–A_2 solution, this stress–strain data is fit to a power-law curve shown in Fig. 2(b). The power-law curve has the Ramberg–Osgood stress–strain relationship as follows:

$$\frac{\varepsilon}{\varepsilon_0} = \frac{\sigma}{\sigma_0} + \alpha\left(\frac{\sigma}{\sigma_0}\right)^n \tag{3}$$

where σ_0 and $\varepsilon_0 = \sigma_0/E$ (here E is the Young's modulus) are the yield stress and the yield strain, respectively, α is a material constant, and n is the strain hardening exponent. The curve–fit gives $n = 5$, and, $\alpha = 4.6$. The other material properties are; $E = 200$ GPa, $\sigma_0 = 248$ MPa, and the Poisson's ratio $\nu = 0.29$.

In this study, J $(= J^{\text{local}})$ calculated by ABAQUS hereinafter denotes the local J-integral throughout the text. The stress values to be analyzed are taken throughout the thickness in the range $1 \leqslant r/(J/\sigma_0) \leqslant 5$.

3. Numerical results and analysis

3.1. Stress field for the deep square specimen

Fig. 3 shows the radial distributions of σ_{rr} and $\sigma_{\theta\theta}$ obtained from FEA and the J–A_2 solution at $\theta = 0°$ at the mid-plane $(z/t = 0)$ for the deep square specimen. Plane-strain HRR field, plane-stress HRR field, and 2D plane-strain FEA results under SSY condition (hereinafter called 2D results) are also shown in Fig. 3. All the stress components are normalized by the yield stress and are plotted against the normalized distance, $r\sigma_0/J$. Three loading levels, 62%, 74%, 80% of the limit load, are considered as the remote loads and these result in $J/(B\sigma_0) = 0.0012$, 0.0038, 0.0081, respectively, at the mid-plane. Limit load is calculated from the assumption of plane-strain condition. Under the loading levels less than 62%, the stress distributions are the same as that of 62% loading level shown in Fig. 3. A_2 is determined using a point match technique as following; (1) The FEA stress value at a point (r, θ) close to the crack front is determined and (2) then the FEA stress value is set to equal to the three-term analytical result to yield the A_2 value. The characteristic length parameter is chosen as the specimen thickness, B. Specifically σ_{rr} and $\sigma_{\theta\theta}$ at $r \approx 1.5$ (J/σ_0), $\theta = 0°$ are used to determine an average A_2 for all the data presented in this paper. Both HRR fields and the three-term solution are determined from the tabulated results of Chao and Zhang (1997). Fig. 4 depicts the angular distributions of σ_{rr}, $\sigma_{\theta\theta}$ and $\sigma_{r\theta}$ at the mid-plane $(z/t = 0)$ with $r\sigma_0/J = 2$.

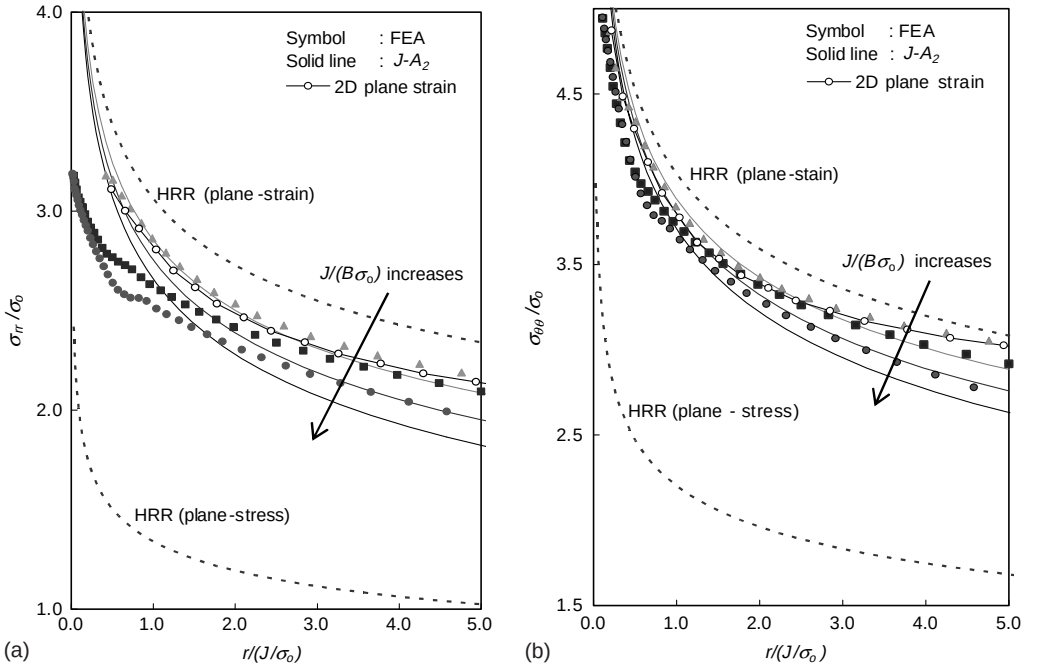

Fig. 3. Variation of stresses with normalized radial distance at $\theta = 0°$ at the mid-plane ($z/t = 0$) for the deep square SENB specimen with $a/W = 0.5$ (a) σ_{rr}, (b) $\sigma_{\theta\theta}$: $J/(B\sigma_0) = 0.0012$, 0.0038, 0.0081 and the corresponding $A_2 = -0.546, -0.560, -0.567$, respectively.

Figs. 3 and 4 show that, at the mid-plane, the J–A_2 solutions match very well with the FEA results along the angular and radial directions within the interested range of $1 \leqslant r/(J/\sigma_0) \leqslant 5$. All the FEA stress results for σ_{rr}, $\sigma_{\theta\theta}$ and $\sigma_{r\theta}$ fall between plane-strain HRR field and plane-stress HRR field. When the load is small, 3D FEA results are same as 2D results, but they deviate from 2D results as the load increases because of the relaxation of crack-front constraint.

The radial distributions of σ_{rr} and $\sigma_{\theta\theta}$ at $\theta = 0°$ at the plane near the free surface ($z/t = 0.49$) are plotted in Fig. 5, while the angular distributions of σ_{rr}, $\sigma_{\theta\theta}$ and $\sigma_{r\theta}$ at $r\sigma_0/J = 2$ are shown in Fig. 6. Compared with the stress distributions at the center plane in Fig. 3, FEA results at the plane near the free surface show great relaxation on the crack–front constraint. Though the plane stress condition is expected to be dominant at the free surface, FEA results at $z/t = 0.49$ are well represented by the J–A_2 solution that is based on the plane strain condition. Under large load, the stress fields are close to plane-stress HRR field and some stresses are below the plane-stress HRR field in $r\sigma_0/J > 2$.

3.2. Stress field for the rectangular specimen

Fig. 7 plots the radial distributions of σ_{rr} and $\sigma_{\theta\theta}$ obtained from FEA and the J–A_2 solution at $\theta = 0°$ at the mid-plane ($z/t = 0$) for the rectangular specimen. Three loading levels, 37%, 62%, 74% of the limit load, are considered and these result in $J/(B\sigma_0) = 0.0007$, 0.0031, 0.0156, respectively, at the mid-plane. In order to cover the scattered fracture toughness data that will be dealt discussed later, different loading levels from those of the deep square specimen are used. Similar to the deep square specimen, plane-strain HRR field provides the upper bound and plane-stress HRR field provides the lower bound in Fig. 7. 3D FEA results are much closer to plane-strain HRR field than to plane-stress HRR field. The angular distributions of σ_{rr}, $\sigma_{\theta\theta}$ and $\sigma_{r\theta}$ at $r\sigma_0/J = 2$ show the same trend as in Fig. 4. Fig. 7 indicates that all the normalized FEA

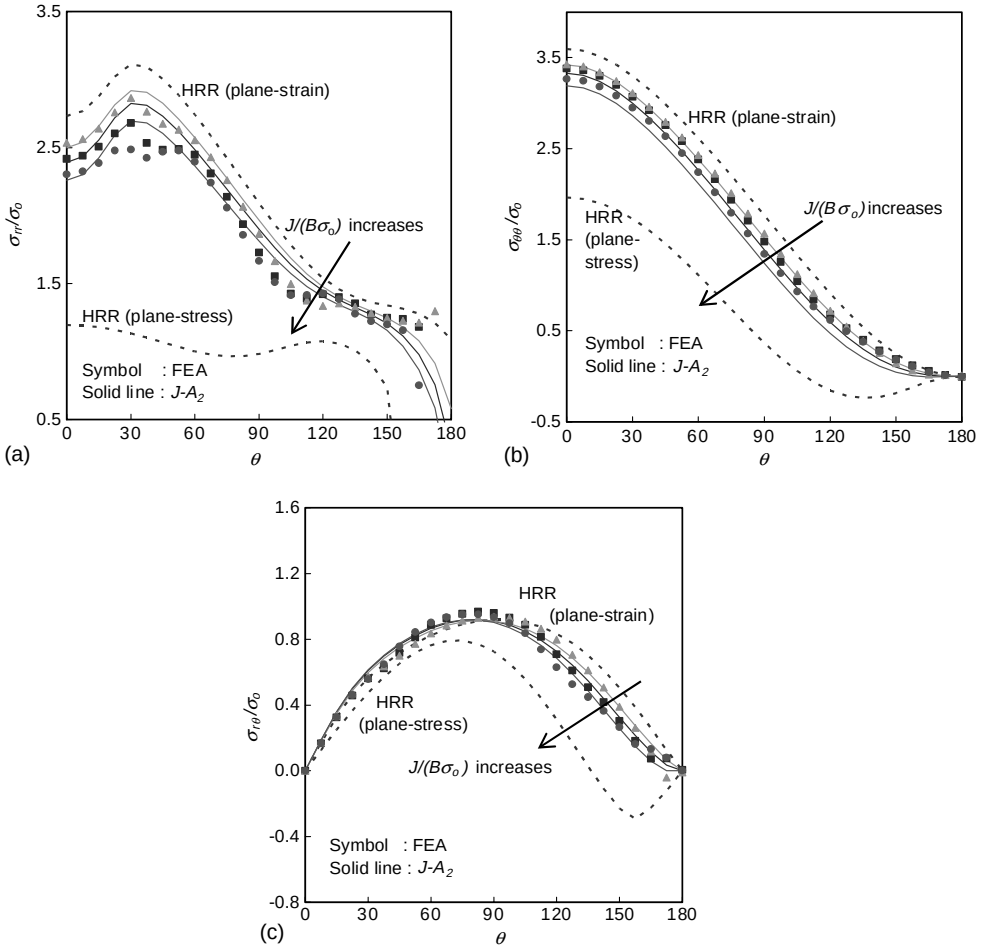

Fig. 4. Angular distribution of stresses at $r\sigma_0/J = 2$ at the mid-plane ($z/t = 0$) for the deep square SENB specimen with $a/W = 0.5$ (a) σ_{rr}, (b) $\sigma_{\theta\theta}$, (c) $\sigma_{r\theta}$: $J/(B\sigma_0) = 0.0012$, 0.0038, 0.0081 and the corresponding $A_2 = -0.546, -0.560, -0.567$ respectively.

results are nearly the same from low to high loads and they are represented well by a single J–A_2 solution within the range of $1.0 \leqslant r/(J/\sigma_0) \leqslant 5.0$. Compared to the deep square specimen, the rectangular specimen does not show any relaxation of crack-front constraint as the load increases. Also the FEA results almost coincide with 2D plane-strain results. It implies that the effect of thickness and magnitude of loading on crack-front constraint can be ignored and the FEA results can be well represented by 2D results for the rectangular specimen. The radial and angular stress distributions at the plane near the free surface for the rectangular specimen have the same tendency as the deep square specimen shown in Figs. 5 and 6.

3.3. Stress field for the shallow square specimen

Fig. 8 plots the radial distributions of σ_{rr} and $\sigma_{\theta\theta}$ obtained from FEA and the J–A_2 solution at $\theta = 0°$ at the mid-plane ($z/t = 0$) for the shallow square specimen. Three loading levels are 17%, 20%, 22% of the limit load and the corresponding normalized loads are $J/(B\sigma_0) = 0.0024$, 0.0106, 0.0230. Similar to the results from the deep square and rectangular specimens, plane-strain HRR field provides the upper bound

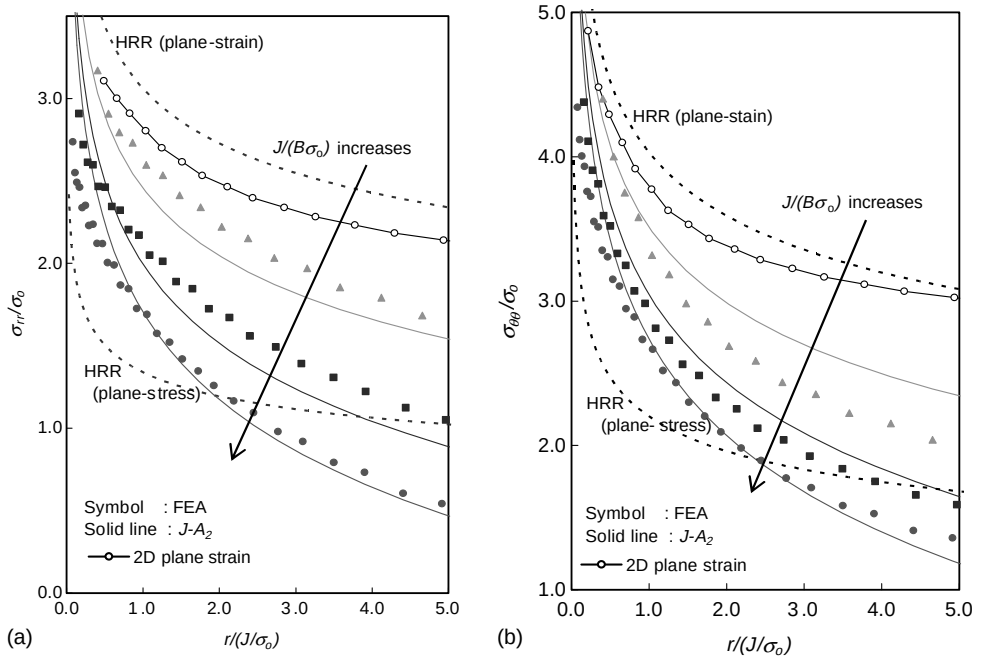

Fig. 5. Variation of stresses with normalized radial distance at $\theta = 0^\circ$ at the plane near the free surface ($z/t = 0.49$) for the deep square SENB specimen with $a/W = 0.5$ (a) σ_{rr}, (b) $\sigma_{\theta\theta}$: $J/(B\sigma_0) = 0.0006, 0.0015, 0.0030$ and the corresponding $A_2 = -1.319, -1.541, -1.529$, respectively.

and plane-stress HRR field provides the lower bound. The angular distributions of σ_{rr}, $\sigma_{\theta\theta}$ and $\sigma_{r\theta}$ at $r\sigma_0/J = 2$ show the same trend as found for the deep square specimen. The deep square specimen shows that the crack-front field resembles 2D results under the high ratio of applied load to limit load ($P/P_L \sim 0.62$). But FEA results for the shallow square specimen deviate early from 2D results under the low loading ratio ($P/P_L \sim 0.17$). This can be considered as one of the characteristics of the shallow cracked specimen; i.e., crack-front constraint is released at a lower load than that of the deep cracked specimen. Though the radial and angular stress distributions at the plane near the free surface for the shallow square specimen are not shown here, relatively good agreement is observed between FEA results and the J–A_2 solution.

3.4. Fracture parameters through thickness

Through-thickness variations of J at the crack front for the deep square, rectangular, and shallow square specimens are shown in Fig. 9(a)–(c) respectively. Under low load, all the specimens show that J is nearly constant through most part of the thickness and decreases slightly toward the free surface. As the load increases, the difference of J at the center and at plane near the free surface becomes prominent and J decreases rapidly near the free surface. Under high load, for the deep square and shallow square specimens, J at the quarter plane ($z/t = 0.25$) is slightly higher than at the center plane but it decreases drastically toward the free surface. The rectangular specimen however shows that, under high load, J has the maximum at the center plane and decreases gradually toward the free surface.

Through-thickness variations of A_2 for the deep square, rectangular, and shallow square specimens are shown in Fig. 10(a)–(c) respectively. For the deep square and shallow square specimens, A_2 remains

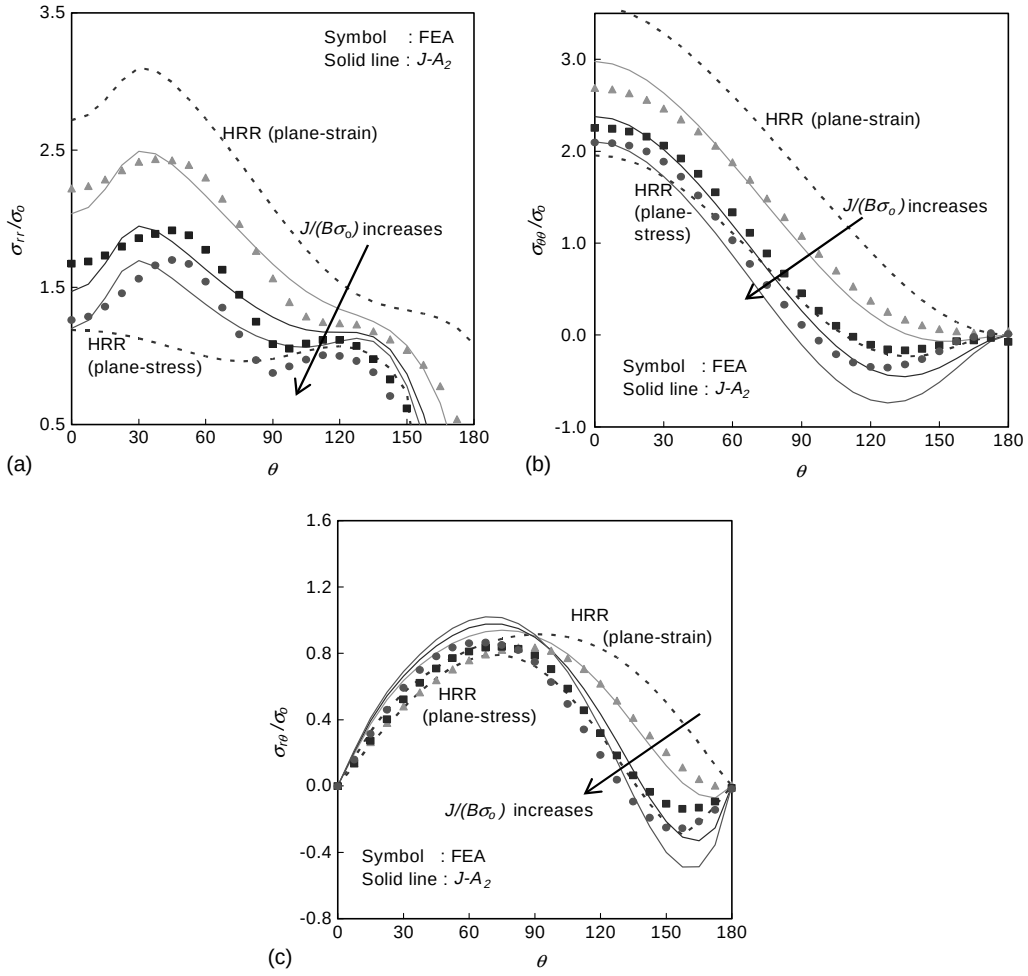

Fig. 6. Angular distribution of stresses at $r\sigma_0/J = 2$ at the plane near the free surface ($z/t = 0.49$) for the deep square SENB specimen with $a/W = 0.5$ (a) σ_{rr}, (b) $\sigma_{\theta\theta}$, (c) $\sigma_{r\theta}$: $J/(B\sigma_0) = 0.0006,0.0015,0.0030$ and the corresponding $A_2 = -1.319,-1.541,-1.529$, respectively.

relatively constant through the thickness, and only decreases at the region near the free surface. Under low load, the shallow square specimen shows that A_2 increases slightly from the center plane to the quarter plane ($z/t = 0.25$) and then decreases drastically toward the free surface. The rectangular specimen shows the gradual decrease from the maximum A_2 at the center plane toward the free surface. From the distribution of A_2 along the crack front, most of the high constraints are expected to occur at the center plane and relatively constant throughout the thickness except near the free surface.

Through-thickness variations of normalized opening stress, $\sigma_{\theta\theta}/\sigma_0$, at a radial distance in the range of $1.0 \leqslant r/(J/\sigma_0) \leqslant 5.0$ ahead of the crack tip are shown in Fig. 11(a)–(c) for the deep square, rectangular and shallow square specimens, respectively. For all the specimens, the opening stress at the mid-plane remains relatively constant or shows a slight increase at the quarter plane ($z/t = 0.25$). But it decreases quickly as the free surface is approached. The rectangular specimen shows that, under high load, $\sigma_{\theta\theta}/\sigma_0$ has maximum at the center plane and decreases gradually toward the free surface. It should be noted that the stress drop

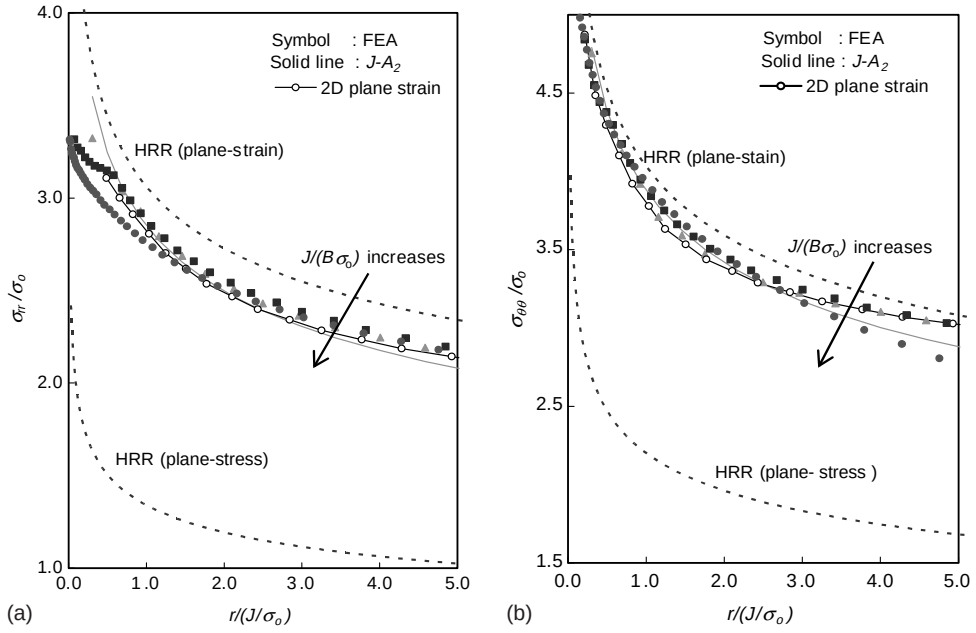

Fig. 7. Variation of stresses with normalized radial distance at $\theta = 0°$ at the mid-plane ($z/t = 0$) for the rectangular SENB specimen with $a/W = 0.5$ (a) σ_{rr}, (b) $\sigma_{\theta\theta}$: $J/(B\sigma_0) = 0.0007,0.0031,0.0156$ and the corresponding $A_2 = -0.625$.

at the region near the free surface is much larger than that caused only by the decrease of J. In addition to J, relaxation of the crack-front constraint contributes this stress drop as well. It can be said that the fracture parameter A_2 efficiently represents the constraint effect on the elastic–plastic crack-front stress fields for SENB specimens throughout the thickness.

4. Relationship between crack-front constraint and cleavage fracture toughness

Having the conclusion from Section 3 that the J–A_2 solution can characterize the 3D crack-front stress fields, we investigate the fracture toughness within the framework of J–A_2. The aim is to demonstrate that the parameter A_2 can be used to quantify the constraint level for various specimen sizes and crack depth in cleavage fracture.

4.1. Failure curves

The failure curves based on J–A_2 theory that are supposed to control the cleavage fracture are derived from the experimental data of the rectangular and shallow square specimens. These specimens are chosen because the rectangular specimen shows the highest crack-front constraint and the shallow square specimen shows the lowest constraint. The failure curves are based on the RKR model proposed by Ritchie et al. (1973); that is "cleavage fracture occurs when the maximum principal stress ahead of a crack tip exceeds a critical value over a characteristic distance". Detail procedures for the J–A_2 based failure curve are outlined in Chao et al. (1994) and Chao and Lam (1996).

Fig. 12 shows the fracture toughness data of the rectangular and shallow square specimens for A36 steel at the temperature of −45 °F that were measured by Sorem et al. (1989) and Wellman et al. (1988).

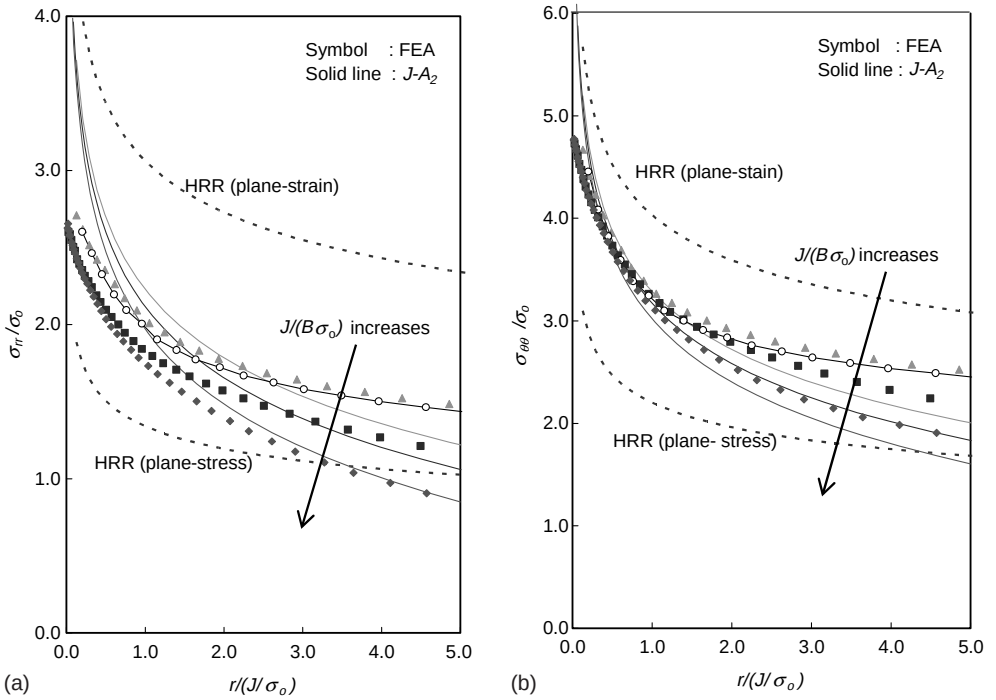

Fig. 8. Variation of stresses with normalized radial distance at $\theta = 0°$ at the mid-plane ($z/t = 0$) for the shallow square SENB specimen with $a/W = 0.15$ (a) σ_{rr}, (b) $\sigma_{\theta\theta}$: $J/(B\sigma_0) = 0.0024, 0.0106, 0.0230$ and the corresponding $A_2 = -1.19, -0.93, -0.86$, respectively.

In Fig. 12, the fracture toughness data are represented in J–A_2 space; x-axis is the A_2 value from the J–A_2 solution and y-axis is the J_c at the center plane. As the highest stress occurs around the center plane for both specimens, J_c at the center plane is chosen for this plot. It was reported that experimental data shown in Fig. 12 are the cleavage fracture with no macroscopic fibrous tearing but they are in the region where linear elastic theory (K_{IC} validity limits according to ASTM E399-83) does not apply (Sorem et al., 1989). Fracture toughness data, J_c, are from the tabulated results in Sorem's dissertation (Sorem, 1989). In this work, FEA is performed for each of the test specimen to obtain the opening stress ahead of the crack tip at $J = J_c$. Then, according to the procedures described in Section 3.1, A_2 value corresponding to the J_c is determined from the opening stress distribution. In Fig. 12, triangular symbols represent the experimental data for the rectangular specimen and circles represent for the shallow square specimen.

As test data has scatter, the experimental fracture toughness data is bounded by lower and upper bound failure curves that are derived from each of the minimum and maximum fracture toughness. In Fig. 12, two pairs of the minimum fracture toughness (J_c, A_2), (25 kJ/m^2, −0.43) for the rectangular specimen and (85 kJ/m^2, −0.84) for the shallow square specimen are used to generate the lower bound failure curve. Substituting these two values into Eq. (1), the fracture toughness parameters are obtained as $\sigma_c/\sigma_0 = 2.63$ and $r_c = 0.77$ mm. With these two values, the lower bound failure curve for controlling cleavage fracture is written as

$$\frac{\sigma_c}{\sigma_0} = \left(\frac{J_c}{\alpha\varepsilon_0\sigma_0 I_n L}\right)^{1/(n+1)} \left[\left(\frac{r_c}{L}\right)^{s_1} \tilde{\sigma}_{\theta\theta}^{(1)}(0) + A_2\left(\frac{r_c}{L}\right)^{s_2} \tilde{\sigma}_{\theta\theta}^{(2)}(0) + A_2^2\left(\frac{r_c}{L}\right)^{s_3} \tilde{\sigma}_{\theta\theta}^{(3)}(0)\right] \tag{4}$$

This lower bound failure curve is shown as the solid line in Fig. 12 which represents the lowest possible fracture toughness for A36 steel assuming that the fracture is controlled by the opening stress ahead of the crack tip. Similarly, the upper bound failure curve is generated using the maximum fracture toughness

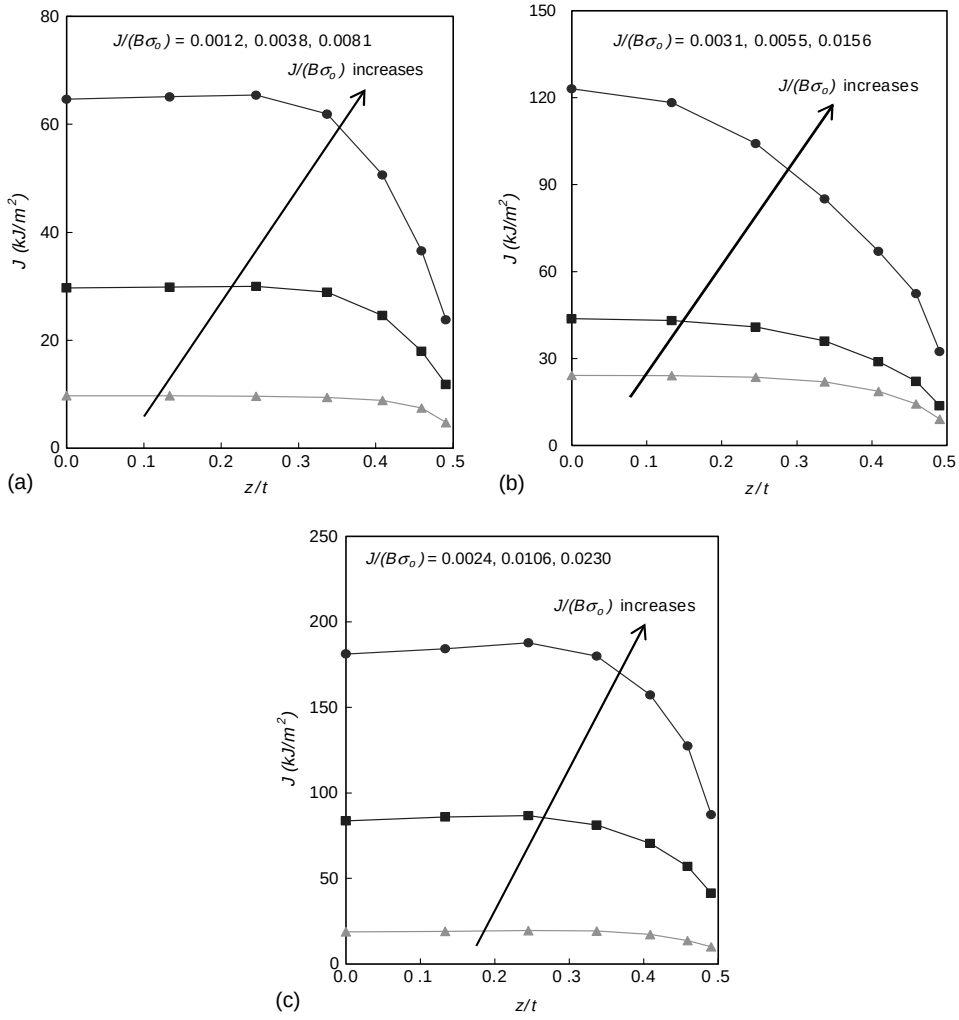

Fig. 9. Variation of J through the thickness (a) the deep square SENB specimen, (b) the rectangular SENB specimen (c) the shallow square SENB specimen.

(J_c, A_2) at (43 kJ/m^2, −0.32) and (186 kJ/m^2, −0.80), and the fracture toughness parameters are determined as $\sigma_c/\sigma_0 = 2.87$ and $r_c = 1.0$ mm. The upper bound failure curve is shown as the dashed line in Fig. 12. These two failure curves are expected to represent the failure behavior of any flawed structures made of this material; i.e., cleavage fracture would occur if (J, A), the applied J and the crack-front constraint A_2, is located between these two curves.

4.2. Prediction of the fracture toughness of the deep square specimen

For the purpose of demonstrating the failure curves, the fracture toughness of the deep square specimen is predicted with the failure curves generated in the previous section. Fig. 13 compares the experimental data of the deep square specimen that were measured by Sorem (1989) with the prediction by the failure curves. The fracture toughness data for the deep square specimen are well captured by the failure curves as

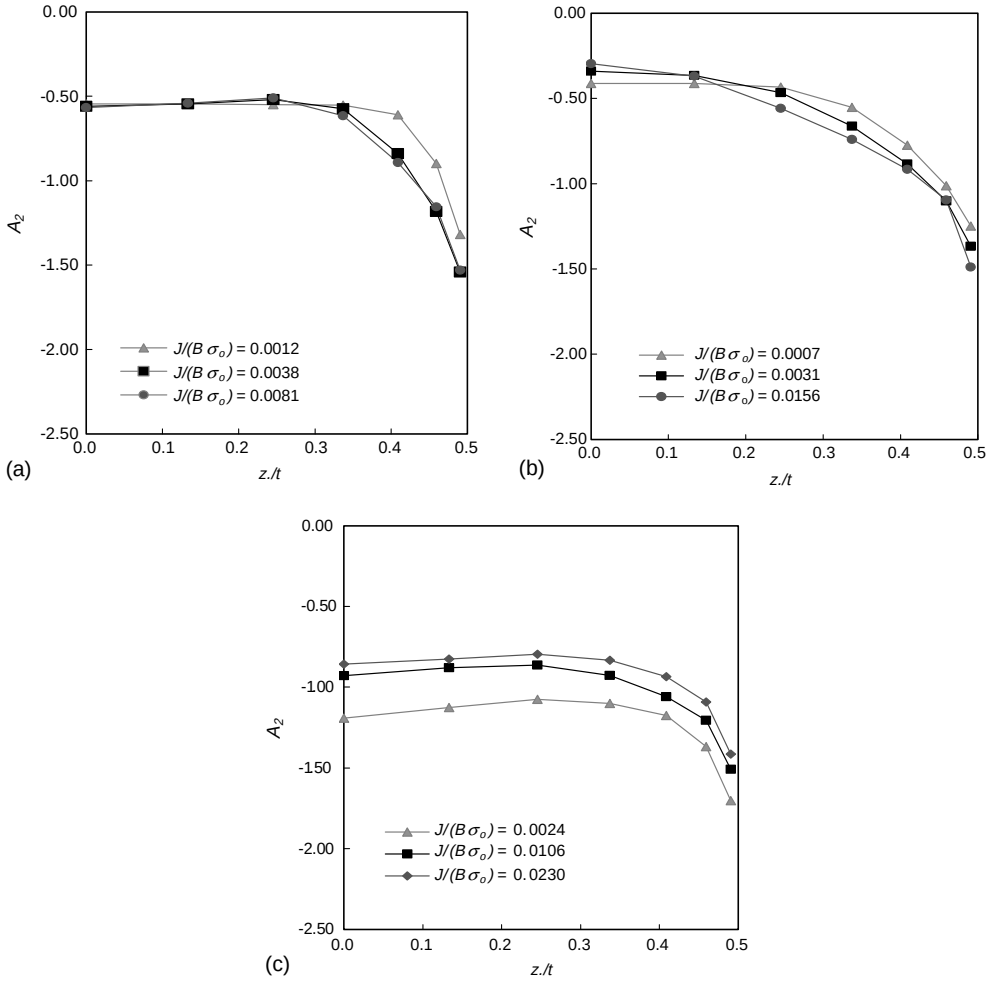

Fig. 10. Variation of A_2 through the thickness (a) the deep square SENB specimen, (b) rectangular SENB specimen, (c) the shallow square specimen.

shown in Fig. 13. It can be concluded that the J–A_2 fracture criterion appears to predict well the effect of crack depth and specimen size on cleavage fracture.

4.3. Fracture toughness and scatter band

In Fig. 14, the opening stress distributions at the crack front are plotted at the applied J equal to the minimum and maximum fracture toughness. Hollow (solid) symbols in Fig. 14 represent the radial distributions of the opening stress when each specimen has the minimum (maximum) fracture toughness. It shows that crack opening stress distributions are nearly the same along the ligament when specimens have the minimum or maximum fracture toughness. This observation is in line with the RKR model on cleavage fracture which postulates that fracture would occur as the opening stress in front of the crack reaches a critical value regardless of the specimen size and crack depth. Even though all the specimens show the

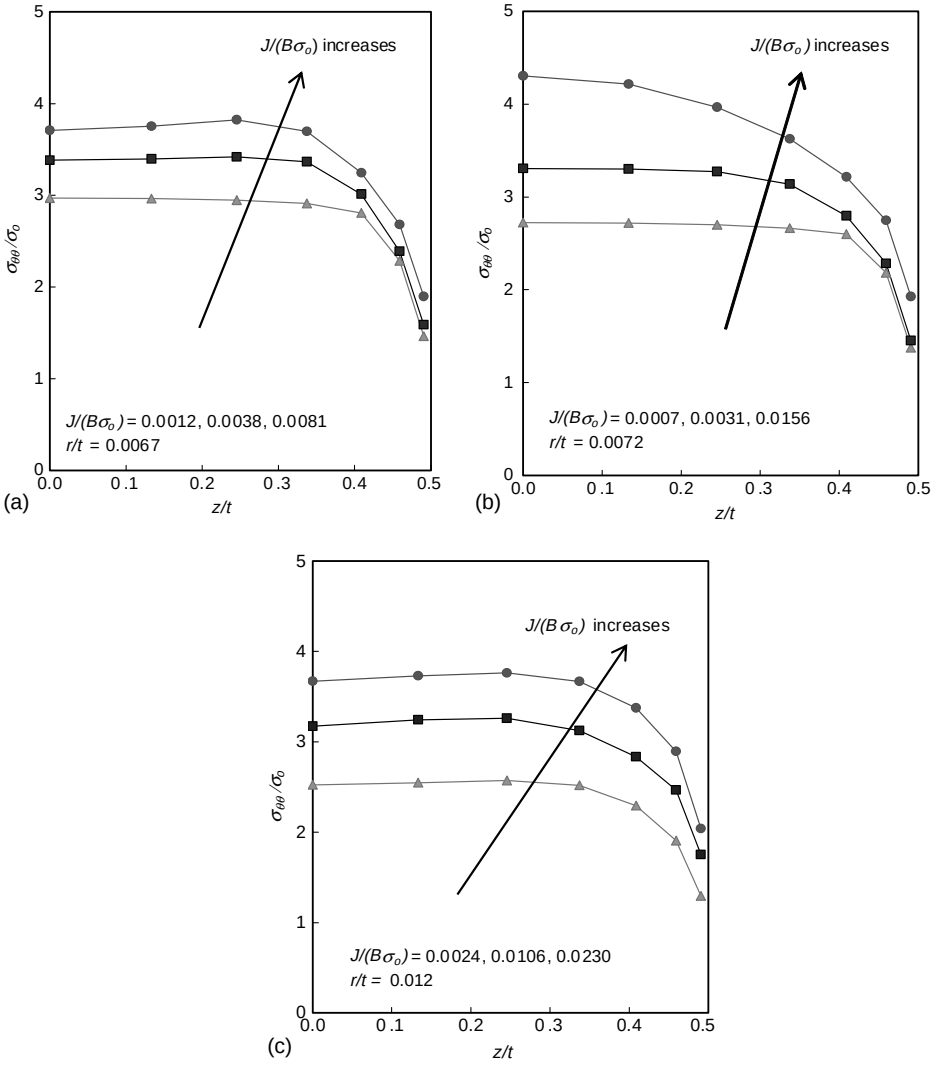

Fig. 11. Variation of $\sigma_{\theta\theta}/\sigma_0$ through the thickness (a) the deep square SENB specimen, (b) the rectangular SENB specimen, (c) the shallow square SENB specimen.

different scattering, Fig. 14 indicates that the crack opening stress distributions are nearly identical at their minimum and maximum critical J or fracture toughness.

Fig. 15 illustrates the fracture toughness data and the difference of J_c between the minimum and maximum toughness values for all the specimens. The rectangular specimen shows a relatively small range of scatter, the deep square specimen shows the substantial increase of scatter, and the shallow square specimen has the most scatter. In Fig. 7(b), the normalized opening stress field for the rectangular specimen is found nearly the same as 2D results over a wide load range. Therefore, 2D plane-strain results can be considered as the opening stress fields for the rectangular specimen. For the deep square specimen at the minimum fracture toughness, the stress field is not much different from the 2D results (see the case of $J/(B\sigma_0) = 0.0038$ in Fig. 3(b)). This is why the minimum fracture toughness for these two specimens are

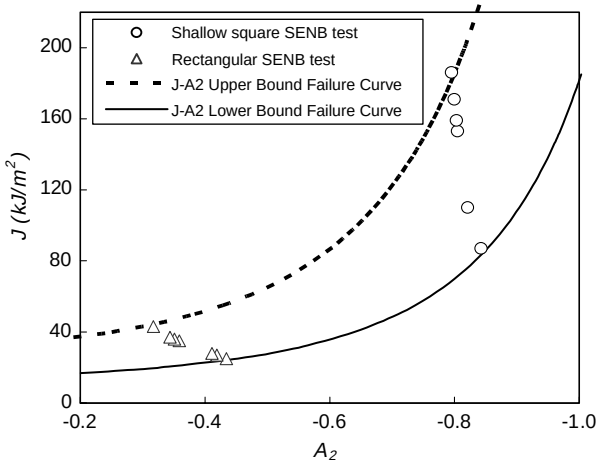

Fig. 12. Failure curves for A36 steel at −45 °F.

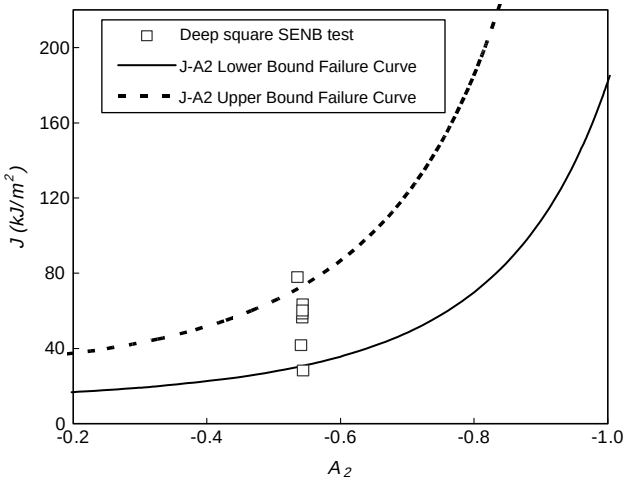

Fig. 13. Comparison of experimental fracture toughness data with the prediction for the deep square SENB specimen.

close as shown in Fig. 15. But as the load increases, the deep square specimen shows relaxation of constraint at the crack front. So, in order to achieve the same stress level as that of the rectangular specimen, more loads and consequently more J should be applied to the deep square specimen. This leads to higher J value as the maximum fracture toughness for the deep square specimen, which is clearly demonstrated by the remarkable difference between ΔJ_1 and ΔJ_2 in Fig. 15. In case of the shallow square specimen, there are composite effect of geometry and loading. Due to the low crack depth ratio, 2D result for the shallow square specimen is far below the plane strain HRR field. In addition to this, the constraint relaxation occurs at the early loading level. These affect the crack-front constraint and let the shallow square specimen have the highest values for the minimum and maximum fracture toughness with the most scattered band (ΔJ_3 in Fig. 15).

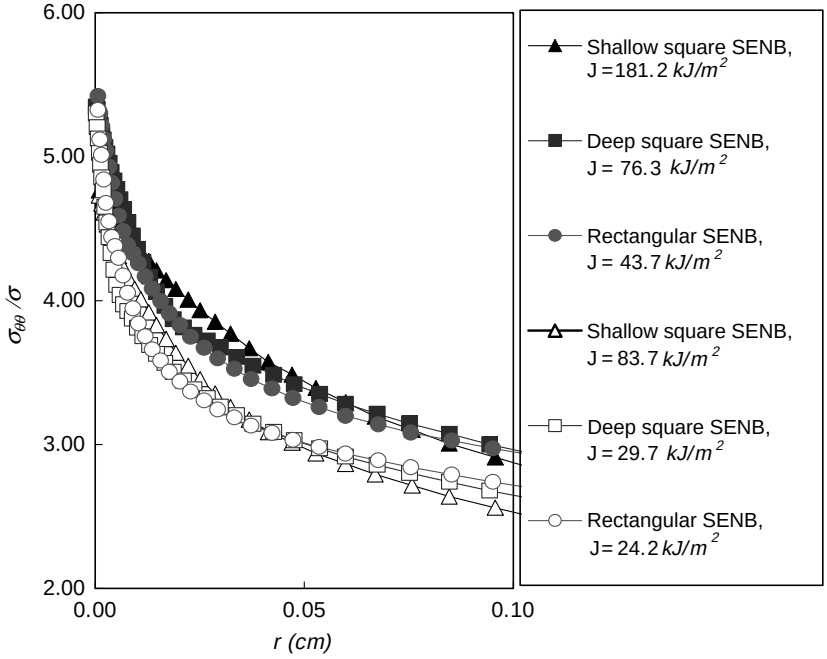

Fig. 14. Comparison of radial distributions of $\sigma_{\theta\theta}/\sigma_0$ at $\theta = 0°$ at the center plane for SENB specimens (Hollow ones represent the opening stresses at the minimum fracture toughness and filled ones at the maximum fracture toughness).

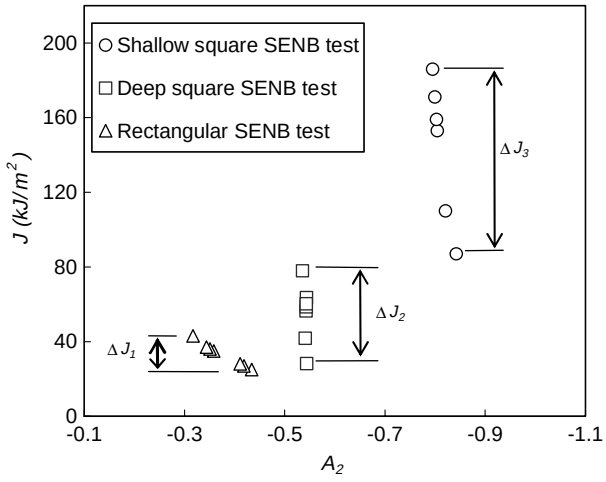

Fig. 15. Comparison of fracture toughness data for A36 steel at −45 °F.

In addition to this qualitative explanation, current study shows that the scatter of data can be quantitatively explained by the crack-front constraint. As shown in Figs. 12 and 13, the different scatters of the fracture toughness data are well captured by the upper and lower bound failure curves based on the crack-front constraint.

4.4. Size-independent fracture toughness

Fig. 7 shows that crack-front fields are well represented by 2D results up to the high level of load for the rectangular specimen. This load level covers the range of the fracture toughness of A36 material at −45 °F. As shown earlier, the deep square and shallow square specimens show a loss of constraint as the load increases. In contrast, the rectangular specimen reveals no sign of relaxation on the crack-front constraint as the load increases. Therefore, the scattering of the toughness data for the rectangular specimens can be attributed only to the variation of material properties. Fracture toughness obtained under these conditions have been considered as size-independent fracture toughness (Dodds et al., 1991; Nevalainen and Dodds, 1995; Koppenhoefer et al., 1995) i.e., insensitive to constraint. No further increase of the specimen size—thickness, width or height—is expected to lower the fracture toughness and reduce scatter band than that of the rectangular specimen unless the specimen geometry and crack depth ratio are changed.

5. Concluding remarks

In order to account for the constraint effects on 3D crack-front fields, detailed elastic–plastic FEA are performed for SENB specimens. Both rectangular and square cross-section of the specimens with a deep crack of $a/W = 0.5$ are considered to investigate the effect of specimen size. A square-cross-section specimen with a shallow crack of $a/W = 0.15$ is also considered to examine the effect of crack depth. FEA results are compared with the J–A_2 three-term solution to check the validity of the parameter A_2 and to quantity the constraint effect for 3D cracks. Also, the scatter behavior of cleavage fracture toughness data is investigated.

The results can be summarized as follows.

(1) For all SENB specimens, FEA results demonstrate different constraint effects on the crack-front stress fields. The square specimens show a loss of constraint as the load increases but the rectangular specimen does not. For the shallow square specimen, the relaxation of constraint begins at lower load than the deep square specimen. In all cases, the J–A_2 solution match well with the 3D stress fields within the interested range of $1 \leqslant r/(J/\sigma_0) \leqslant 5$ at the mid-plane and even at the plane near the free surface.
(2) Values of J, $\sigma_{\theta\theta}$ and A_2 at the crack front along the thickness direction are studied. Generally their maximum values occur at the mid-plane and the minimum at the plane near the free surface. They remain relatively constant along most part of the thickness and drastically decrease at the region near the free surface. Under high load, the rectangular specimen shows the highest value at the center plane which gradually decreases as the free surface is approached.
(3) From comparison of cleavage fracture toughness data, it is found that the crack opening stress is the same for all the SENB specimens at the minimum or maximum fracture toughness. It implies that cleavage fracture is indeed controlled by the opening stress distribution and there is a close relationship between the crack-front constraint and the fracture toughness.
(4) 3D crack-front constraint quantified by J–A_2 solution reveals the relationship between crack-front stress fields, constraint, and fracture toughness. With the introduction of J–A_2 based failure curves, it is shown that the minimum fracture toughness and scatter band can be predicted for the specimens with different constraints. All the fracture toughness data chosen for current study experienced the cleavage fracture without any ductile tearing. However, there was extensive tearing plasticity before fracture and the testing temperature −45 °F is in the lower transition region. Our analysis in the current paper indicates that the J–A_2 solution can be used for characterizing the cleavage fracture toughness in the transition region.

(5) The crack-front stress fields at the mid-plane coincide with 2D stress fields only under small loading conditions. As the load increases, the stress fields for the deep square and shallow square specimens deviate from 2D results considerably but not for the rectangular specimen. This implies that the rectangular specimens are insensitive to the constraint and therefore, fracture toughness values measured from these specimens can be regarded as the size-independent toughness for 3D SENB specimens.
(6) Although the constraint level of SENB specimens with $a/W = 0.15$ and 0.5 cover a wide range of constraint levels, further validation of the theory through comparison with tension dominated specimens, e.g. center cracked tension specimen, would be very meaningful.

References

ABAQUS, 1998. Version 5.8-1, Hibbitt, Karlsson and Sorensen, Inc., Pawtucket, RI.

Betegon, C., Hancock, J.W., 1991. Two-parameter characterization of elastic–plastic crack-tip fields. Journal of Applied Mechanics 58, 104–110.

Chao, Y.J., Lam, P.S., 1996. Effects of crack depth, specimen size, and out-of-plane stress on the fracture toughness of reactor vessel steels. Journal of Pressure Vessel Technology 118, 415–423.

Chao, Y.J., Zhang, L., 1997. Tables of plane strain crack tip fields: HRR and higher order terms. ME-Report97-1, Department of Mechanical Engineering, University of South Carolina.

Chao, Y.J., Zhu, X.K., 1998. J–A_2 characterization of crack-tip fields: extent of J–A_2 dominance and size requirements. International Journal of Fracture 89, 285–307.

Chao, Y.J., Zhu, X.K., 2000. Constraint-modified J–R curves and its application to ductile crack growth. International Journal of Fracture 106, 135–160.

Chao, Y.J., Yang, S., Sutton, M.A., 1994. On the fracture of solids characterized by one or two parameters: theory and practice. Journal of the Mechanics and Physics of Solids 42, 629–647.

Dodds Jr., R.H., Anderson, T.L., Kirk, M.T., 1991. A framework to correlate a/W effects on elastic–plastic fracture toughness (J_C). International Journal of Fracture 88, 1–22.

Hutchinson, J.W., 1968. Singular behavior at the end of a tensile crack tip in a hardening material. Journal of the Mechanics and Physics of Solids 16, 13–31.

Kim, Y., Zhu, X.K., Chao, Y.J., 2001. Quantification of constraint on elastic–plastic 3D crack front by the J–A_2 three term solution. Engineering Fracture Mechanics 68, 895–914.

Koppenhoefer, K.C., Kirk, M.T., Dodds Jr., R.H., 1995. Size and deformation limits to maintain constraint in K_{IC} and J_C testing of bend specimens. In: Constriant Effects in Fracture Theory and Application, Second Volume. ASTM STP 1244. American Society for Testing and Materials, Philadelphia, pp. 445–460.

Nevalainen, M., Dodds Jr., R.H., 1995. Numerical investigation of 3-D constraint effects on brittle in SE(B) and C(T) specimens. International Journal of Fracture 74, 131–161.

O'Dowd, N.P., Shih, C.F., 1991. Family of crack-tip fields characterized by a triaxiality parameter—I. Structure of fields. Journal of the Mechanics and Physics of Solids 39, 989–1015.

O'Dowd, N.P., Shih, C.F., 1992. Family of crack-tip fields characterized by a triaxiality parameter—II. Fracture applications. Journal of the Mechanics and Physics of Solids 40, 939–963.

Rice, J.R., 1968. A path independent integral and the approximate analysis of strain concentration by notches and cracks. Journal of Applied Mechanics 35, 379–386.

Rice, J.R., Rosengren, G.F., 1968. Plane strain deformation near a crack tip in a power-law hardening material. Journal of the Mechanics and Physics of Solids 16, 1–12.

Ritchie, R.O., Knott, J.F., Rice, J.R., 1973. On the relationship between critical tensile stress and fracture toughness in mild steel. Journal of the Mechanics and Physics of Solids 21, 395–410.

Sorem, W.A., 1989. The effect of specimen size and crack depth on the elastic–plastic fracture toughness of a low-strength high-strain hardening steel, PhD dissertation, The University of Kansas, Lawrence.

Sorem, W.A., Dodds, R.H., Rolfe, S.T., 1989. An analytical and experimental comparison of rectangular and square crack-tip opening displacement fracture specimens on an A36. In: Nonlinear Fracture Mechanics: Volume II—Elastic–Plastic Fracture. ASTM STP 995. American Society for Testing and Materials, Philadelphia, pp. 470–494.

Wellman, G.W., Sorem, W.A., Dodds Jr., R.H., Rolfe, S.T., 1988. Specimen thickness effects for elastic–plastic CTOD toughness of an A36 steel. In: Fracture Mechanics: Eighteenth Symposium, ASTM STP 945, American Society for Testing and Materials, Philadelphia, pp. 535–554.

Yang, S., Chao, Y.J., Sutton, M.A., 1993a. Complete theoretical analysis for higher order asymptotic terms and the HRR zone at a crack tip for mode I and mode II loading of a hardening material. Acta Mechanica 98, 79–98.

Yang, S., Chao, Y.J., Sutton, M.A., 1993b. Higher order asymptotic fields in a power law hardening material. Engineering Fracture Mechanics 45, 1–20.

Zhu, X.K., Chao, Y.J., 1999. Characterization of constraint of fully plastic crack-tip fields in non-hardening materials by the three-term solution. International Journal of Solids and Structures 36, 4497–4517.

Zhu, X.K., Kim, Y., Chao, Y.J., Lam, P.S., 2001. Constraint effect on 3-D crack-front stress fields in elastic–plastic thin plates. In: Fatigue and Fracture Mechanics: 33rd Volume. In: Reuter, W.G., Piascik, R.S. (Eds.), ASTM STP 1417. ASTM International, West Conshohocken, PA, pp. 270–287.